AIAA JOURNAL
Vol. 48, No. 7, July 2010

Effect of Interaction Strength on Unsteadiness in Turbulent Shock-Wave-Induced Separations

Louis J. Souverein,* Pierre Dupont,† Jean-François Debiève,† and Jean-Paul Dussauge‡
Université de Provence, 13013 Marseille Cedex 13, France
and
Bas W. van Oudheusden§ and Fulvio Scarano¶
Delft University of Technology, 2629 HS Delft, The Netherlands

DOI: 10.2514/1.J050093

The effect of the interaction strength on the unsteady behavior of a planar shock wave impinging on a low Reynolds turbulent boundary layer is investigated. This is achieved by means of a variation in incident shock angle under otherwise constant flow conditions. In addition, the effect of an order-of-magnitude variation in the Reynolds number is considered. This has been done for equivalent interaction strength, based on a similar probability of occurrence of instantaneous flow separations. The measurement technique employed is two-component planar particle image velocimetry. Common mechanisms for the large-scale reflected-shock unsteadiness are deduced by means of conditional statistics based on the separation bubble height. The results indicate that both upstream and downstream mechanisms are at work, the dominant mechanism depending on the interaction strength. No significant dependence on the Reynolds number was observed for interactions with a similar probability of instantaneous flow separations.

Nomenclature

C_f	=	friction coefficient
H	=	height of the interaction
h	=	height of the separation bubble
L	=	length of the interaction
L_{ex}	=	amplitude of the oscillation of the reflected shock
M_e	=	freestream Mach number
p_0	=	stagnation pressure
Re_θ	=	Reynolds number based on the momentum thickness
S_L	=	Strouhal number
T_0	=	stagnation temperature
U_e	=	freestream velocity
U^+_{VD}	=	U_{VD}/u_τ
U_{VD}	=	Van Driest transformed velocity
x	=	longitudinal coordinate
X_0	=	mean position of the reflected-shock foot
X^*	=	$(x - X_0)/L$
y	=	wall-normal coordinate
Y^*	=	y/δ_0
y^+	=	yu_τ/ν
δ_0	=	upstream boundary-layer thickness (99% U_e)
φ	=	incidence angle of the shock generator
ν	=	kinematic viscosity
θ	=	boundary-layer momentum thickness
ρ	=	density
ρ_w	=	density at the wall
u_τ	=	friction velocity

Received 24 July 2009; revision received 11 September 2009; accepted for publication 9 November 2009.

*Research Assistant, Institut Universitaire des Systèmes Thermiques Industriels, Unité Mixte de Recherche, Centre National de la Recherche Scientifique, Groupe Supersonique, 5, rue Enrico Fermi; Delft University of Technology. Member AIAA.

†Chargé de Recherche, Institut Universitaire des Systèmes Thermiques Industriels, Unité Mixte de Recherche, Centre National de la Recherche Scientifique, Groupe Supersonique, 5 rue Enrico Fermi.

‡Directeur de Recherche, Institut Universitaire des Systèmes Thermiques Industriels, Unité Mixte de Recherche, Centre National de la Recherche Scientifique, Groupe Supersonique, 5 rue Enrico Fermi.

§Associate Professor, Faculty of Aerospace Engineering, Kluyverweg 1.

¶Professor, Faculty of Aerospace Engineering, Kluyverweg 1.

I. Introduction

THE effect of a planar shock impinging on a turbulent boundary layer establishes one of the classic interaction phenomena in compressible viscous flow analysis. This particular form of interaction also has a direct technological relevance to the performance of high-speed vehicles, affecting notably the efficiency of supersonic intakes. Furthermore, maximum mean and fluctuating pressure and thermal loads on a structure are most often found in regions of shock-wave/boundary-layer interaction (SWBLI) and are thus important factors in vehicle development. On the other hand, flow control is seen as an important issue in future vehicle design [1], requiring a rigorous physical understanding of the mechanisms behind the phenomenon as well as improved simulation capabilities, neither of which can be attained without fundamental experimental investigations and validation. The renewed attention for the feasibility of sustainable supersonic transport has revived the interest in SWBLI in the moderate supersonic regime. In this context the European sixth framework program UFAST ("Unsteady Effects of Shock Wave Induced Separation") was initiated, in which the shock reflection interaction is one of the flow cases of interest, with an emphasis on closely coupled and mutually validated numerical and experimental investigations [2].

One of the key issues in turbulent SWBLI research is the origin of the low frequency of the large-scale motion of the shock. Frequency spectra of the shock unsteadiness display a development from broadband for mild interaction strength to selective with a clear low-frequency bump for well-separated flows [3]. In addition, there is a debate over the source of the unsteadiness. A correlation has been observed in literature between fluctuations in the upstream boundary layer and the shock foot motion [4–7]. A model relating shock excursions to random turbulence fluctuations has been proposed [8]. These fluctuations have been attributed to low-speed elongated structures with a length of many boundary-layer thicknesses [5,6], leading to the supposition that the shock dynamics are governed by the state of the upstream boundary layer. On the other hand, a mechanism has been proposed in literature that links the time scales of the separation bubble dynamics to the entrainment of mass by the mixing layer and subsequent vortex shedding [3]. These time scales

are of the same order as those observed for the low-frequency shock excursions. Moreover the model explains the change in shock frequency with interaction strength, leading to the supposition that it is the downstream separation bubble that governs the shock unsteadiness. This dependence on the separation bubble dynamics has also been observed in other literature [3,9–15]. In addition, there are indications for the existence of an inherent instability of the mean flow field leading to separation bubble pulsations, which would be in further support of a downstream dependence [15–17]. Finally, indications have been found that the complete reflected shock moves more or less as one shock front with a relatively low frequency, while in addition the foot of the reflected shock also responds at a much higher frequency to the passage of individual large-scale turbulent structures in the boundary layer [18,19]. The debate with respect to origin of low-frequency unsteadiness and the different nature of the observed frequency spectra suggest that a combination of several mechanisms might be at work. Moreover, depending on the strength of the interaction, ranging from incipient separation with no mean flow reversal to well-developed separation with mean reversed flow, a shift in the dominance of each mechanism might occur. In compression ramp flows, it is known that the onset of separation depends mainly on the Mach number and that it is practically independent of the Reynolds number [20].

The aim of the current paper is two-fold. Firstly, it is investigated how the shock unsteadiness mechanisms (upstream or downstream) vary as a function of the imposed shock intensity. Secondly, it is verified whether the role of these mechanisms depends on the Reynolds number for incipiently separated flows for the incident reflecting shock interaction. In the first place, an overview is given of the different experimental conditions, followed by a characterization of the investigated flow cases. Secondly, the role of the separation bubble with respect to the low-frequency shock unsteadiness is considered. This is done by means of conditional statistics based on the instantaneous separation bubble height. It is verified that there is a dependence of the large-scale shock excursions on the occurrence of flow separation. Furthermore, the relation between the state of the incoming boundary layer and bubble height is investigated. In addition, the dependence of the development of large coherent structures in the interaction on the imposed shock intensity is addressed for both cases: incipiently separated and well-separated flow. Finally, a synthesis of the observed mechanisms for the interaction unsteadiness is presented.

II. Experimental Arrangement

The general flow configuration under consideration is that of an oblique shock wave impinging on the turbulent boundary layer of the wind tunnel wall. Particle image velocimetry (PIV) has been employed to obtain instantaneous velocity data. Experiments have been performed for a range of flow deflection angles at a Reynolds number of $Re_\theta = 5000$ and a Mach number of 2.3, and for a single flow deflection angle at a Reynolds number of $Re_\theta = 50,000$ and a Mach number of 1.7.

A. Experimental Facilities

The high Reynolds number experiments ($Re_\theta = 50,000$) were performed in the TST-27 transonic supersonic wind tunnel of the High-Speed Aerodynamics Laboratory at Delft University of Technology (TU Delft). Precise descriptions of the experimental setup and flow conditions have been given in previous publications [18,19].

The wind tunnel has a test section with dimensions 280 × 270 mm (width height). It is a blow-down facility that can operate at Mach numbers ranging from 0.5 to 0.85 and from 1.15 to 4.2 with a unit Reynolds number of 30×10^6 to 130×10^6 m^{-1}, for a run time of up to 300 s. The Mach number is set by means of a continuously variable throat and flexible upper and lower nozzle walls. The stagnation pressure can be set independently with typical values in the range of 2.0 to 3.0×10^5 Pa; the stagnation temperature is determined by the ambient temperature of the storage vessel. The velocity transient inherent to blow-down operation has been determined to be approximately 5×10^{-2} ms^{-2}, corresponding to a stagnation temperature transient of 6×10^{-2} Ks^{-1}. The effect on the mean velocity is less than 1% of the freestream velocity over a complete run duration of 60 s. The freestream turbulence level of the facility was assessed to be about 1%.

The tests were performed at a nominal freestream Mach number of $M_e = 1.69$ ($U_e \approx 450$ ms^{-1}), a stagnation temperature of $T_0 =$ 273 K, and a stagnation pressure of $p_0 = 2.3 \times 10^5$ Pa, resulting in a freestream unit Reynolds number of 35×10^6 m^{-1}. The undisturbed boundary layer was assessed to be in fully developed turbulent condition with a thickness, based on 99% of the external velocity, of approximately $\delta_0 = 17$ mm. The incident shock wave for the SWBLI was generated by a full-span wedge imposing a flow deflection of $\varphi = 6.0$ deg.

The low Reynolds number ($Re_\theta = 5000$) experiments were performed in the supersonic wind tunnel of the Supersonic Group at the Institut Universitaire des Systèmes Thermiques Industriels (IUSTI) in Marseille. Precise descriptions of the experimental setup and flow conditions have been given in previous publications [3,11].

The wind tunnel has a test section with dimensions 170 × 120 mm (width × height). It is a closed-loop continuously running hypoturbulent facility with a Mach number of 2.28 determined by the fixed throat, and a freestream unit Reynolds number of 5.5×10^6 m^{-1}, with a run time of up to four hours. The stagnation pressure can be set independently with typical values ranging from 0.15 to 0.9×10^5 Pa. The stagnation temperature is determined by the ambient air temperature and is kept constant to within 0.2 K/h. The tunnel has a particularly low freestream turbulence level of approximately 0.1% of the freestream velocity.

During the current experimental investigation, the measurement conditions were a nominal freestream Mach number of $M_e = 2.28$ ($U_e \approx 550$ ms^{-1}), a stagnation temperature of $T_0 = 295$ K, and a stagnation pressure of $p_0 = 0.5 \times 10^5$ Pa. A two-dimensional supersonic boundary layer develops on the wind tunnel nozzle wall with a thickness (99% U_e) of approximately $\delta_0 = 11$ mm. The boundary layer on the tunnel floor is subjected to a shock wave produced by a full-span sharp edge plate placed in the external flow. The imposed flow deflection angles ($\varphi = 5.5$, 8.0 and 9.5 deg) produce interactions that range from incipient separation to well-developed separation.

The most relevant flow parameters for both experiments are summarized in Table 1.

B. PIV Setup

The measurement techniques employed during the current investigation are two-component planar particle image velocimetry (2C-PIV) and dual-plane particle image velocimetry (dual-PIV). A large data ensemble was acquired for each investigated flow case (4000–10,000 velocity field realizations) permitting conditional statistical analyses.

The high Reynolds number data set was acquired using dual-PIV, designed to obtain locally time-resolved PIV data. The principle of dual-PIV depends on the mutually independent operation of two 2C-PIV systems. Both systems are aligned to provide illumination in the same measurement plane while observing identical fields of view using two cameras. The specifications of the setup of the dual-plane system and its data validation are provided in previous work [18,19].

Table 1 Aerodynamic parameters of the flow upstream of the interaction

Experiment	M_e	U_e (ms^{-1})	δ_0 (mm)	Re_θ	C_f	T_0 (K)	θ (mm)	δ^* (mm)
High Re	1.7	450	17	5×10^4	1.5×10^{-3}	273	1.39	3.3
Low Re	2.3	550	11	5×10^3	2.1×10^{-3}	295	0.96	3.4

In the original investigation, several experimental data sets were acquired for different time delays, with the purpose of extracting time-correlation information. In the current research, advantage was taken of the large data ensemble size to perform conditional statistics.

Measurements were made in the TU Delft's facility, in the vertical (streamwise–wall-normal) symmetry plane of the test section. The illumination was provided by a Spectra-Physics Quanta Ray laser (400 mJ pulse energy and a 6 ns pulse duration) and a Quantel laser (300 mJ pulse energy and a 9 ns pulse duration). Both are double-pulsed Nd:Yag lasers with a wavelength of 532 nm. The light sheet thickness was approximately 2 mm. The flow was seeded with liquid DEHS (Di(2-ethylhexyl)sebacate) droplets, dispersed in the settling chamber of the wind tunnel by means of a seeding rake using a PIVTEC aerosol generation device. The estimated effective particle size is about 1 μm, with an estimated time response constant of 2 μs [21]. The particle images were recorded at 12-bit with a resolution of 1376×1040 pixel using a PCO Sensicam QE and a LaVision Imager Intense QE, both equipped with a Nikon $f = 60$ mm lens, diffracting with $f_{\#} = 8$. Of the charge-coupled devices (CCDs) only 992 pixels were used in the vertical direction given the aspect ratio of the interaction region of interest. The flow was imaged over a field of view of approximately $4\delta_0 \times 3\delta_0$ in streamwise and wall-normal direction, respectively, at a digital resolution of 55.1 μm/pixel. The timing and data acquisition were performed by LaVision Davis 7.2 in combination with a PTU 9 (programmable timing unit). Recordings were made at an acquisition rate of 5 Hz. The pulse separation was kept constant at 1.5 μs for both laser systems, producing particle displacements of approximately 0.7 mm (corresponding to 12 pixels) in the freestream flow. The image pairs were interrogated using the WIDIM algorithm [22], employing correlation window deformation with an iterative multigrid scheme, at a 31×31 pixels window size (1.7×1.7 mm) and an overlap factor of 75%. This resulting measurement grid resolution is 0.43 mm/vect in both the X and Y direction. The total ensemble size is approximately 4000 realizations.

The low Reynolds number data sets were acquired using 2C-PIV in the IUSTI's supersonic wind tunnel. Details for the setup of the system are provided in previous work [3,23]. Measurements were made in the vertical (streamwise–wall-normal) symmetry plane of the test section. The illumination was provided by a double-pulsed ND:YAG laser New Wave Solo 2, which delivers 30 mJ per pulse. The light sheet thickness is 1 mm. Incense smoke was used to seed the boundary layer. After decantation of the smoke, the particles were injected from the wall, upstream of the wind tunnel nozzle. As the wind tunnel stagnation pressure is subatmospheric, the particles are naturally drawn into the flow. The estimated time constant of the particle response is 4.5 μs [24], which corresponds to diameters of 0.5 μm. The particle images are recorded by Flowsense 10 bit cameras with CCD size of 1600×1200 pixels, equipped with Nikon Macro Nikkor $f = 60$ mm objectives with the diaphragm set to $f_{\#} = 2.8$. Images were recorded at 8 bit with an effective sensor size adapted to the field of view under consideration. The recordings were made using Flowmanager 4.71 software via the Dantec Flowmap System Hub, at an acquisition rate of 12 Hz.

The data set at a flow deflection angle of 5.5 deg was acquired using a single camera. The CCD was cropped to a size of 1600×800 for a useful data range of approximately $4.4\delta_0 \times 1.5\delta_0$ in streamwise and wall-normal direction, respectively, at a digital resolution of $\approx$27 μm/pixel, yielding a field of 97×78 vectors. It is noted that the height of the useful data domain for the low Reynolds case is limited by the vertical extent of the seeded part of the flow, which is typically $\frac{y}{\delta_0} < 1.5$. A pulse separation of 1 μs was employed, producing particle displacements of approximately 0.6 mm. The images were interrogated using the DynamicStudio software, using an iterative approach and applying a Gaussian weighting function to the interrogation windows. The final window size is 64×32 pixels pixels with an overlap factor of 75%, yielding a PIV data resolution of 0.43×0.21 mm/vect in the X and Y directions, respectively. The total ensemble size is 5000 realizations.

The data sets for the 8.0 and 9.5 deg flow deflection angles were obtained using the same PIV system but at a two-times-lower magnification factor, and employing two side-by-side cameras in panoramic mode for the 9.5-deg case. The useful data range is approximately $8.5\delta_0 \times 1.5\delta_0$ for the 8.0 deg data set and $17\delta_0 \times 1.5\delta_0$ for 9.5 deg. In both cases, the final interrogation window size is 32×16 pixels with an overlap factor of 75%, yielding a PIV data resolution of 0.48×0.24 mm/vect in the X and Y directions, respectively. The total ensemble size for each data set is 10,000 realizations.

The settings of the parameters to process the PIV data have been optimized in such a way that the nondimensional spatial resolution is approximately identical. Indeed, the PIV interrogation window sizes for low Reynolds interactions in the IUSTI facility and the high Reynolds interaction in the TUD wind tunnel yield a nondimensional cell size of $\frac{\Delta y}{\delta_0} \simeq 2$–$2.5 \times 10^{-2}$ in all cases.

C. Flow Characterization

The incoming boundary-layer profiles, derived from PIV measurements, are shown in Fig. 1 for both Reynolds number cases. Considering the mean velocity profile, the first evident effect of the higher Reynolds number is to increase the fullness, as can be inferred from Fig. 1a. A second consequence is the larger extent of the log-law region, going up to $y^+ = 3000$ for the high Reynolds number in comparison to $y^+ = 200$ for the low Reynolds number (see Fig. 1b). The friction velocity was obtained by making a least-squares fit to the log law of the wall of the measured velocity profile. This was done for different values of the second log-law constant C, choosing the value that yields the best slope fit ($C = 7$ for the high Reynolds number case vs $C = 5.25$ for the low Reynolds number case, as indicated by the vertical shift in Fig. 1b). For both Reynolds number cases, the log law extends to about the same height in external scaling ($\frac{y}{\delta_0} = 0.3$). The velocity fluctuations (turbulence levels) in the boundary layer are shown in Fig. 1c in Morkovin scaling. This representation takes into account the density profile and the wall friction $\rho_w u_\tau^2$, where the subscipt w refers to the wall conditions [25]; no significant differences are observed between both flows. Deviations between the profiles fall within the dispersion observed for other measurements [25] (figure 1.6 of the reference). It may hence be concluded that in both cases we are dealing with a canonical zero-pressure gradient supersonic ($M < 5$) turbulent boundary layer.

Turning our attention to the general flow organization of the different interactions, it can be seen in Fig. 2 that the interactions display a large qualitative similarity. The high Reynolds number interaction is shown in Fig. 2a, displaying contours of the mean vertical velocity component superimposed on the divergence of the velocity field. The latter highlights strong compression and expansion regions within the flow, such as shocks and expansion waves, inducing large density variations and a nonzero divergence. The boundary-layer profile and the boundary-layer edge are also shown for reference. The figures for the low Reynolds number, Figs. 2b–2d, represent schlieren visualizations. In all cases, the incident shock wave impacts on the boundary layer, causing a thickening thereof. A reflected shock forms upstream of the extrapolated impact point of the incident shock. The incident shock on the contrary reflects as an expansion fan, which in turn interacts with the reflected shock in the potential flow region. A classical evolution of the interaction is observed from the incipient to the separated cases [26]. In particular, the expansion fan becomes attached to the reflected shock for the incipiently separated flows, with a shock crossing point that becomes immersed in the boundary layer. It is remarked that the low Reynolds interaction at 5.5 deg shows a large topological similarity to the high Reynolds number case.

The interaction length L will be selected as the relevant longitudinal length scale. It is defined as the distance between the mean location of the reflected-shock foot and the extrapolated intersection point of the incident shock with the wall. Correspondingly, the dimensionless longitudinal coordinate is defined as $X^* = (x - X_0)/L$, where X_0 is the mean position of the reflected-shock foot.

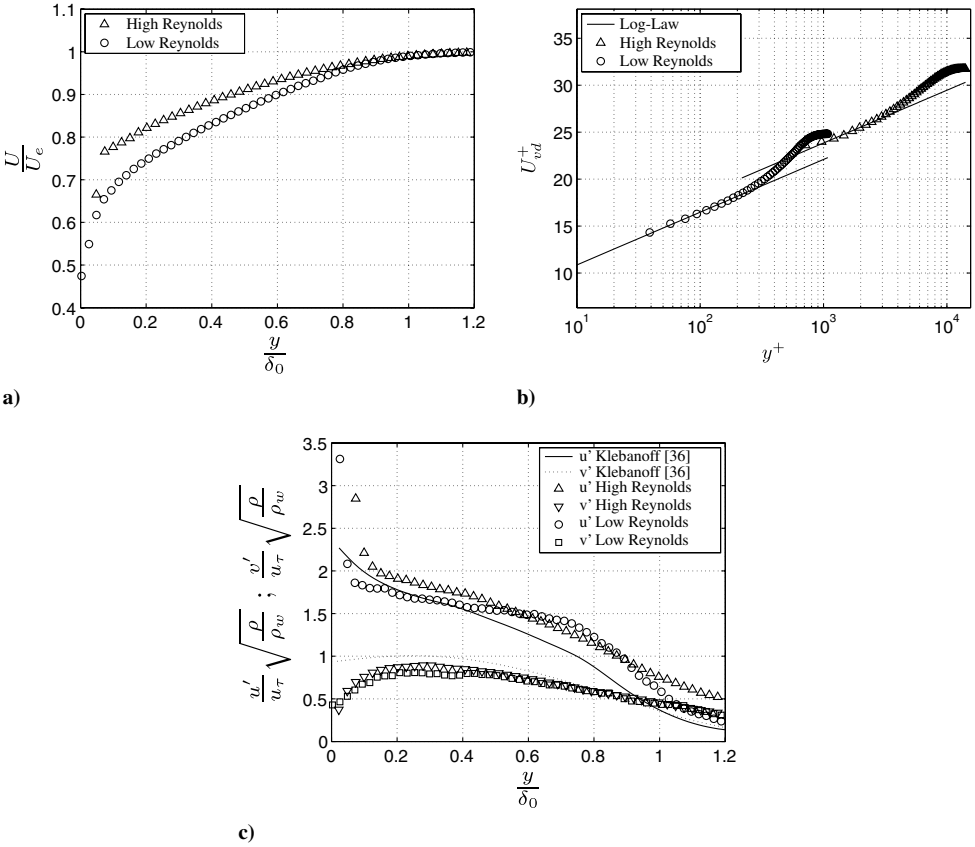

Fig. 1 Incoming boundary-layer characterization: a) nondimensional mean streamwise velocity, b) mean velocity profile in Van Driest scaling with the log-law fit, and c) nondimensional velocity fluctuations with Klebanoff reference profile [36].

Table 2 gives an overview of the interaction characteristics: the interaction length, the interaction length normalized by the boundary-layer thickness, the measured shock excursion length [taken from the current PIV data sets for 6.0 and 5.5 deg (see Sec. IV) and from hot wire measurements reported in literature [11] for 9.5 deg], and the theoretical height of the interaction. The latter is defined as $\frac{H}{L} = \frac{1}{2}\tan(\beta)$, with β the incident oblique shock angle, assuming that the incident and the reflected shock have the same angles with respect to the wall (rather than with respect to the local preshock flow direction), which in is a reasonable approximation for the interactions considered here. For the considered cases, $\frac{H}{L}$ depends principally on the Mach number and only weakly on the

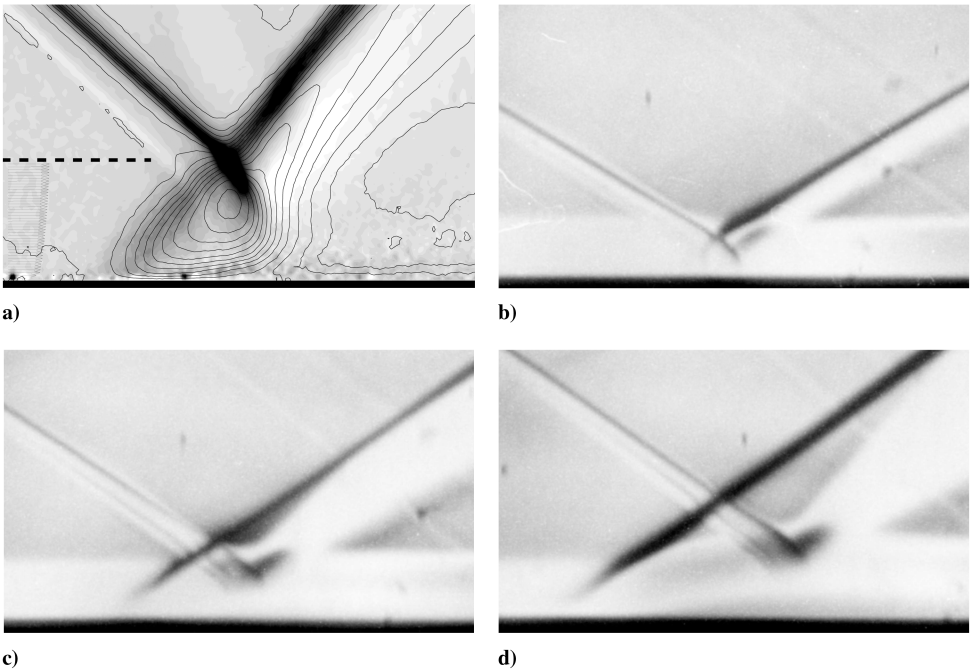

Fig. 2 Interaction visualization for the four flow cases: high Reynolds number a) $\varphi = 6.0$ deg and low Reynolds numbers b) $\varphi = 5.5$ c) $\varphi = 8.0$, and d) $\varphi = 9.5$ deg.

Table 2 Interaction length comparison

Experiment	High *Re*	Low *Re*		
Flow deflection (deg)	6.0	5.5	8.0	9.5
L (mm)	37	25	46	71
L/δ_0	2.2	2.3	4.2	6.5
L_{ex}/L	0.2	0.2	-	0.1
H/L	0.45	0.30	0.32	0.34

flow deflection angle. This is a purely geometrical effect, the shock wave being steeper for the lower Mach number. Indeed, it can be remarked that the interaction height increases by 50% for the Mach 1.7 high Reynolds number case as compared with the Mach 2.3 low Reynolds number case. This can be inferred from Fig. 2: the shock angle is larger at Mach 1.7 (see Fig. 2a) than at Mach 2.3 (see Fig. 2b). Therefore, when comparing L_{ex}, care has to be taken of the flow topology on either side of shock crossing point. Hence, all values for the excursion length have been obtained at the same nondimensional height ($\frac{y}{H} = 1.56$), corresponding to the height $\frac{y}{\delta_0} = 3.45$ for the 9.5 deg interaction [11]. It has been verified that the same result is obtained from hot-wire- and PIV-based data.

III. Characterization of Instantaneous Flow Separation

In previous studies [3,23], in the case of low Reynolds number shock reflection with substantial separation on the mean, the low-frequency shock motions were related to the low-frequency pulsation of the separation bubble. The latter was associated, as in subsonic separations [27,28], to the flapping of the mixing layer, which develops downstream of the reflected shock and which corresponds to the shear region between the relatively slow-moving flow in the separation bubble and the fast-moving fluid outside it. The associated time scale was derived by means of a simple model based on the entrainment process in the mixing layer [3]. However, it was shown [19] that also an interaction of the incipient type still displays unsteady shock movements that occur at frequencies that are one to two orders of magnitude below those present in the incoming boundary layer. In this case, flow separation occurs only intermittently without a well-developed separation bubble on the mean, but evidence for shedding of large-scale vortices was shown. Given the existence of similar mechanisms, it will therefore be investigated if features in common with the mean separated flows can be found for the separation events.

In the present investigation the effect of shock strength on the interaction behavior is investigated, as well as the effect of Reynolds number for two equivalent incipient shock-induced separations. Two quantitative criteria were used for the definition of the equivalence of the interaction strength between the two Reynolds number cases. They are based on the probability and extent of the occurrence of flow reversal. In the first place the isocontours of the flow reversal probability were considered, giving an indication of the intermittency of the flow separation. In the second place, the maximum height of the instantaneous dividing streamline was determined for each realization, giving an indication of the separation bubble height. This leads to the selection of a low Reynolds number interaction corresponding to a 5.5 deg flow deviation as the interaction with a strength equivalent to the high Reynolds number case with a 6.0 deg flow deflection. The unsteadiness properties of the flow separation for the different interactions are described in detail in the next sections.

A. Probability of Reversed Flow

Figure 3 shows the probability of the instantaneous occurrence of flow separation for each point in the flow domain, computed as the ratio of the number of realizations with reverse flow over the total number of realizations. The isocontours of the vertical mean velocity are superimposed on the figure. To visualize the subsonic region of the interaction, the mean sonic line is also reported. It has been obtained using the modified Crocco–Busemann relation assuming adiabatic wall conditions [29]. It can be seen that the probability of flow separation increases with the shock strength. For the smallest shock strength (5.5 deg low Reynolds and 6.0 deg high Reynolds), the flow reversal occurs in less than half of the realizations, which is consistent with the fact that no mean separation bubble is observed. The low Reynolds number case is statistically very similar to the

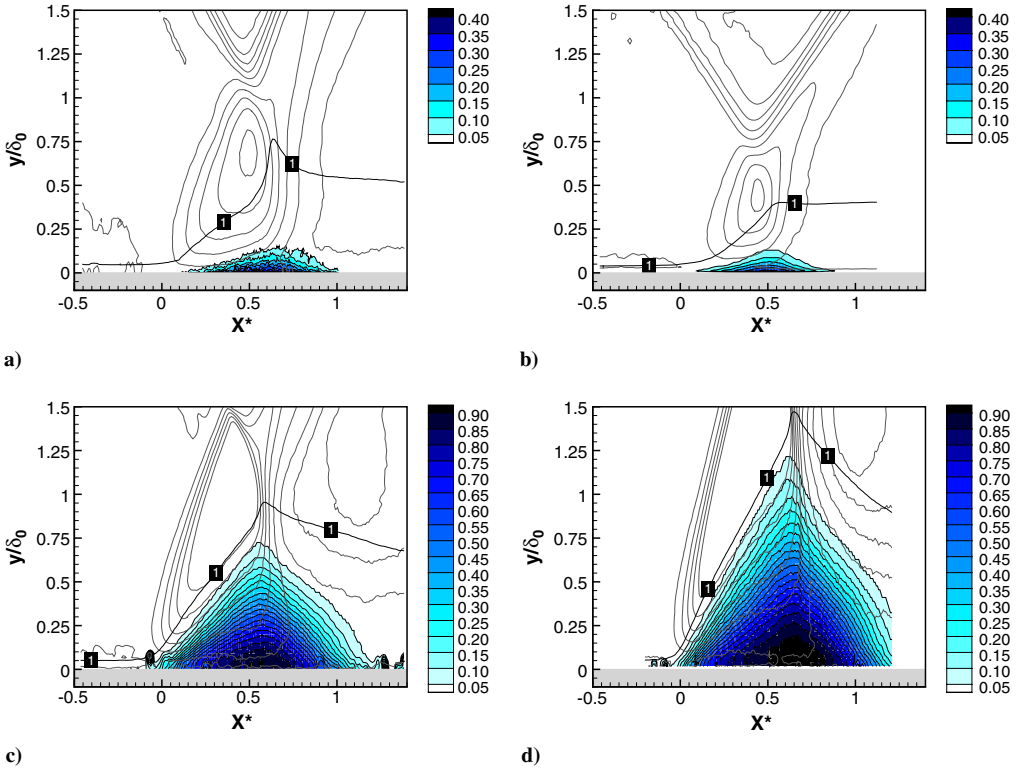

Fig. 3 Flow reversal isoprobability contour levels: high Reynolds number a) 6.0 deg and low Reynolds number b) 5.5, c) 8.0, and d) 9.5 deg. Isocontour lines of the vertical velocity component are shown for reference. The solid black line, labeled *1*, indicates the approximate mean sonic line.

high Reynolds number case. Both display a probability of reversed flow of approximately 40% and a reversed flow region with similar horizontal and vertical extent when normalized by the interaction length and the boundary thickness, respectively. At 8.0 deg, flow reversal occurs locally in 90% of the realizations, and for 9.5 deg in 95% of the realizations.

In all cases, downstream of the interaction, the sonic line remains elevated (around $y/\delta_0 \approx 0.5$ for the incipient cases and $y/\delta_0 \approx 1$ for the separated cases). The sonic line has only a very slight slope towards the wall: in the relaxation part, more than the half of the boundary layer is subsonic, and it remains so for many boundary-layer thicknesses downstream of the interaction. It is clear from Fig. 3 that the sonic line and the shock intersection in the low Reynolds number cases are shifted upwards for increasing deflection angle. In addition, the separation bubble height increases.

B. Bubble Height Statistics

In the previous paragraph, it was confirmed that both incipient cases present similar probability of reverse flow. Here, it will be verified that the separation bubble also corresponds to a similar organization of the flow. The instantaneous dividing streamline, defined as the set of points $y_j(x)$ where $\int_0^{y_j(x)} u\,\mathrm{d}y = 0$, will be determined for each realization in accordance with previous work [3]. The main limitation of this procedure is to neglect the density variations in the low-velocity part of the interaction. However, this assumption is thought to have limited effect on the final conclusion for adiabatic flows. The instantaneous maximum elevation of the dividing line will be denoted h. Of course, when no reverse flow is observed, h is zero by definition.

The histogram of this maximum bubble height h (the vertical axis is normalized by the total number of realizations) is shown in Fig. 4. It can be observed that the height of the separation bubble increases with increasing interaction strength. For the weakest interactions, the separation bubble does not exist all of the time, the flow being fully attached in a significant part of the realizations (see Figs. 4a and 4b). Strict equality between the two histograms was of course difficult to obtain. Nevertheless, the histogram of the high Reynolds number case looks similar to the one for the 5.5 deg shock angle. For the larger interaction strengths, a separation bubble is practically always present: a substantial separation bubble of over a quarter of the boundary-layer thickness in height can be observed to be present at all time (see Figs. 4c and 4d).

Therefore, the two incipient cases seem to have comparable flow separation states and organizations; this will be examined in a more detailed way in the following section.

IV. Comparison of the Interaction Characteristics

A comparison is made between the shock-induced incipient separations at low Reynolds number (5.5 deg) and at high Reynolds number (6.0 deg), including the low Reynolds separated cases (8.0 and 9.5 deg) that have already been analyzed [3,11]. The conventional streamwise scaling with the interaction length is used to represent the horizontal coordinates in terms of X^*, as mentioned in Sec. II.C. As the vertical dimensionless coordinate, $y^* = y/L$ is chosen. Using this scaling, the mean and fluctuating flow organization show great similarity for the different flow cases (incipient and well-separated) (see Figs. 5 and 6). The crossing between the incident and reflected shock occurs in the vicinity of $y/L \approx 0.3$ in the

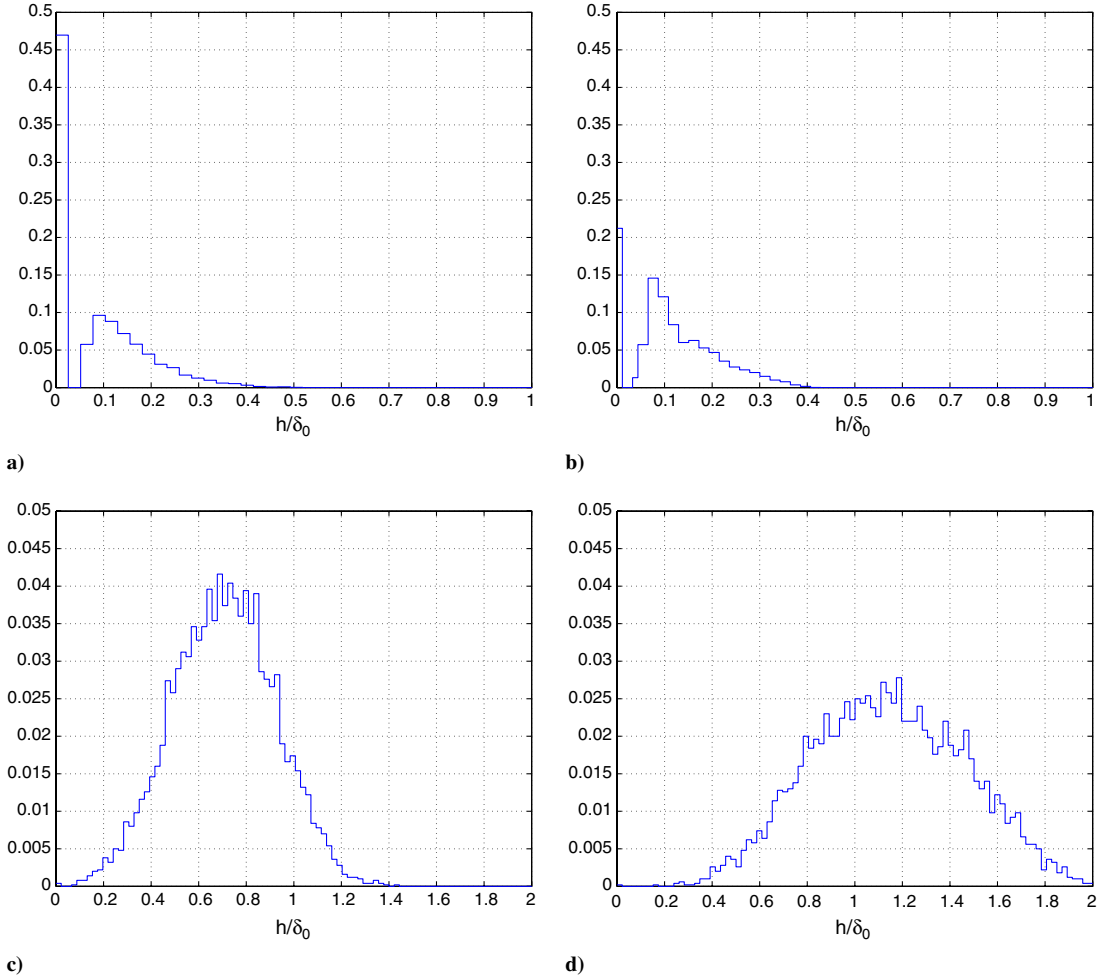

Fig. 4 Separation height histograms: high Reynolds number a) 6.0 deg, low Reynolds number b) 5.5 deg, and low Reynolds number separated cases c) 8.0 and d) 9.5 deg.

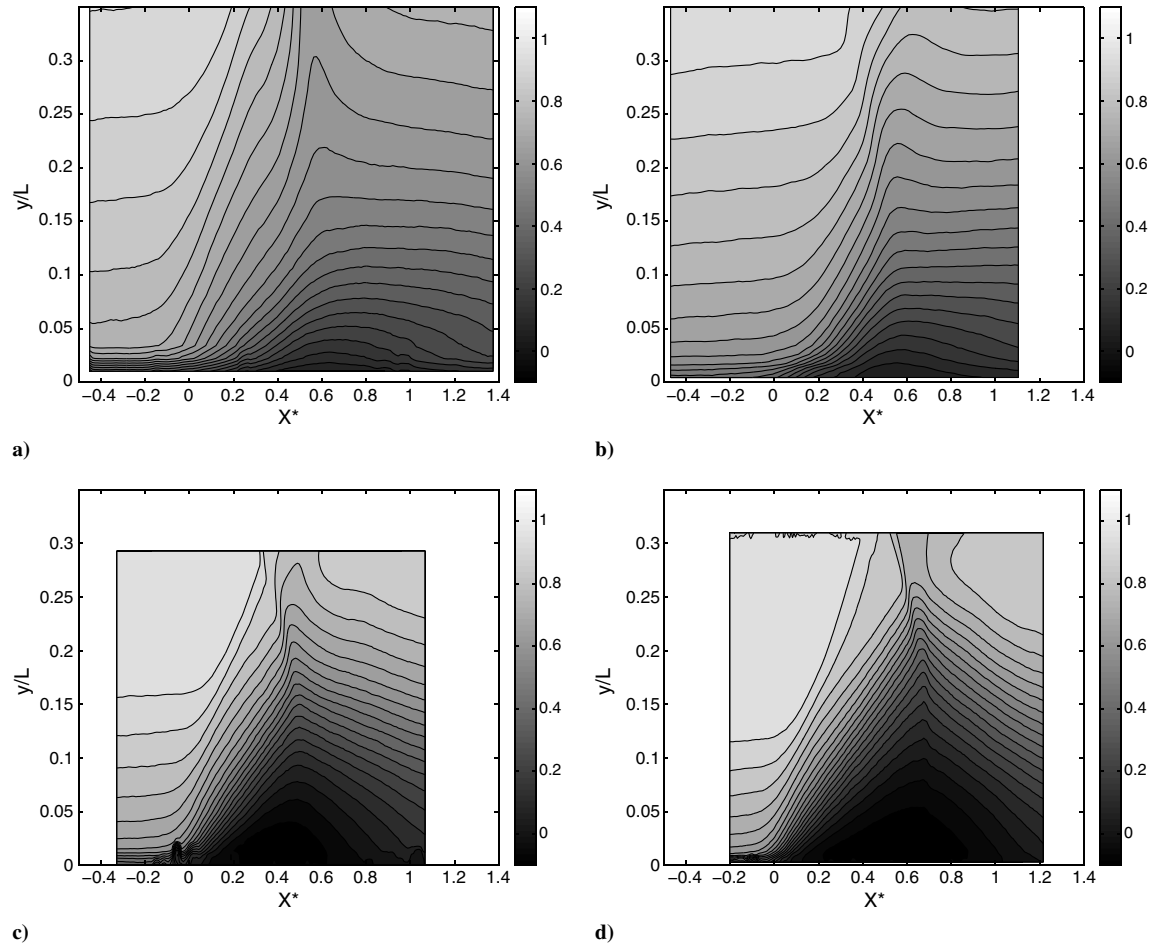

Fig. 5 Mean U component: high Reynolds number a) 6.0 deg, low Reynolds number b) 5.5 deg, and low Reynolds number separated cases c) 8.0 and d) 9.5 deg.

$M = 2.3$ low Reynolds cases and of $y/L \approx 0.45$ in the $M = 1.7$ high Reynolds one.

As can be seen from Fig. 5, no mean flow reversal occurs in either of the incipient cases. From Fig. 5a it can be observed that there is more high-velocity fluid close to the wall in the incoming boundary layer for the high Reynolds number case, which is consistent with the fuller boundary-layer profile (see Sec. II.C).

Figure 6 shows that in all cases, increased U-component fluctuations occur starting from the reflected-shock foot, which is consistent with the development of vortical structures. This region of high turbulence intensity develops between $0 < X^* < 0.5$ along an inclined path (see the white lines in Fig. 6). The angle of the line with the horizontal is comparable for the two incipient cases and increases strongly for the separated cases. As a consequence, the region of high turbulence intensities extends up to $y/L \approx 0.1$ for the incipient cases and up to $y/L \approx 0.2$ in the separated cases. In the separated cases, this region of high levels of turbulence was associated with the development of a mixing layer in the first part of the interaction, followed by the shedding of large vortices, as in subsonic flow separation [3,11,23]. It will be shown in Sec. V.D that a similar behavior is observed in the incipient separations as well. For all cases, the region of high turbulence intensity is advected in the downstream reattached boundary layer.

If the global organization of the flow fields looks very similar between the two incipient cases, a major difference can be observed concerning the reflected shock in the boundary layer (i.e., $y/\delta_0 < 1$ or $y/L < 0.5$). Figure 6a shows a clear imprint of a well-defined shock for the high Reynolds number case down to $y/L \approx 0.1$, whereas the shock is hardly distinguishable in the low Reynolds incipient case. Indeed, for the latter case, the reflected shock appears as a continuous velocity decrease rather than a well-defined step in the turbulent part of the flow, this notwithstanding the smoothing effect introduced by the particle lag in the PIV measurements. Hence, the reflected-shock foot constitutes a fan of compression waves rather than a well-defined shock wave (see Fig. 6b). Such a dependence of the separation shock on the Reynolds number was already observed in the case of compression ramps, both from experiments and direct numerical simulation [14,30,31]. With increasing interaction strength, the reflected shock becomes better defined, as can be observed for the low Reynolds 8.0 deg case (see Fig. 6c). This is confirmed for the largely separated low Reynolds case (9.5 deg), which exhibits a well-defined reflected shock, as in the high Reynolds incipient case (see Fig. 6d).

In all cases, the reflected shock is clearly unsteady. This is best illustrated from the longitudinal evolution of the root-mean square (RMS) of the V-component fluctuations (see Fig. 7). The amplitude of the oscillation of the reflected shock (L_{ex}) can be estimated from the width of the peak of the RMS fluctuations. For the incipient cases, the region under the point of shock crossing is in the turbulent boundary layer and it becomes difficult to identify a well-defined peak, in particular in the low Reynolds case, where the shock is smeared. If measurements above the crossing point are considered, for example at $y/H = 1.56$, the length L_{ex} can be estimated for all cases. When a width criterion based on $1/e$ of the maximum peak height is used, an estimated shock oscillation amplitude of $L_{ex} \approx 0.2L$ is inferred for the incipient cases, compared with $L_{ex} \approx 0.1L$ for the separated cases. These values are also reported in Table 2. In the high Reynolds case, the measurements are significantly more affected by optical effects related to the large density jump across the shock. This is known to lead to measurement artifacts in the vicinity of the shock waves [32,33]. For example, the incident shock measurements generate significant RMS levels despite the fact that it is most likely stationary, as is the case with the first peak of the high Reynolds number case in Fig. 7. Therefore, the L_{ex} could be

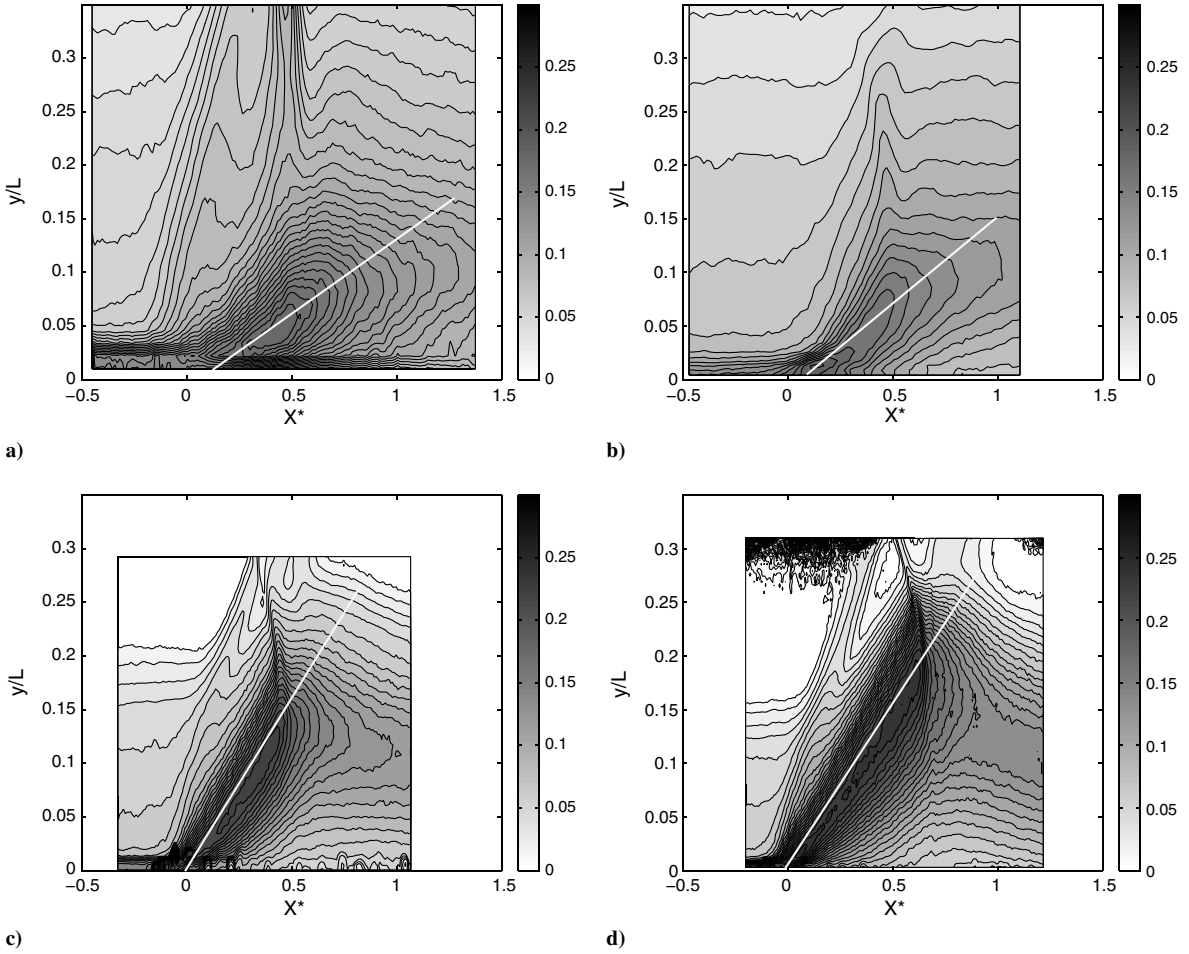

Fig. 6 *U*-component fluctuations: high Reynolds number a) 6.0 deg, low Reynolds number b) 5.5 deg, and low Reynolds number separated cases c) 8.0 and d) 9.5 deg. Fluctuation values are normalized by the freestream velocity. The white lines indicate the approximate path of the peak turbulence intensity within the first part of the interaction.

overestimated for the high Reynolds number case with respect to the low Reynolds measurements. Nevertheless, the RMS peak for the reflected shock is significantly wider and higher than the peak for the incident shock, which is a direct consequence of the unsteadiness of the reflected shock. The RMS caused by the unsteadiness is larger than the measurement uncertainties. The determination of the oscillation amplitude is therefore thought to be sufficiently reliable for the present purposes.

The results support the notion that the selected incipient shock-induced separations are also equivalent from the perspective of interaction flow unsteadiness. Therefore, in the following part, it will be attempted to identify whether the mechanisms behind this unsteadiness are also of a similar nature. This will be done in the first place by concentrating on the unsteadiness of the interaction zone, based on the existence of instantaneous flow reversal. The possible links between the reflected-shock excursions and the upstream boundary-layer unsteadiness will be addressed and compared with results already obtained in the separated cases. In addition, the development of large-scale coherent structures, a proposed mechanism for the separation bubble pulsation, will be investigated for the cases without mean flow reversal.

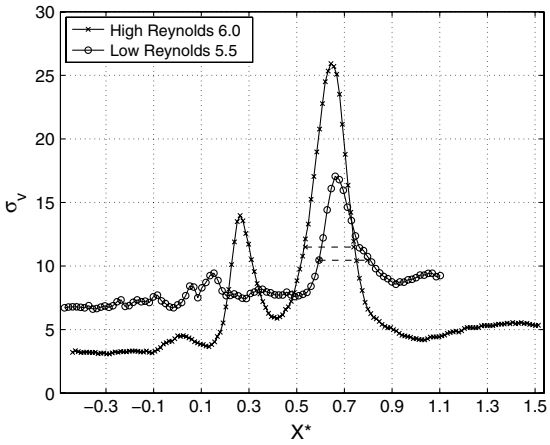

Fig. 7 Longitudinal evolution of the RMS normal velocity fluctuations across the shocks for the two incipient cases ($y/H = 1.56$).

V. Conditional Analysis Based on Separation Bubble Height

In the previous part, we have shown that significant differences exist between the turbulence fields of the incipient and separated cases: in both cases there is evidence of new energetic structures developing downstream of the reflected-shock foot, but an important variation is observed in the energy peak level and in the vertical extent. In the separated cases, these new turbulent scales have been related to the development of a mixing layer in the interaction [11,23], leading to the shedding of large vortices downstream of $X^* = 0.5$. In the incipient cases, a similar organization is not intuitively evident, as no mean separation occurs. Nevertheless, the probability to observe separated flow remains large (see Fig. 3). Therefore, conditional analysis based on the instantaneous existence of a reversed flow has been carried out, similar to that already performed for the separated cases [3].

Three cases will be considered: shallow, medium, and thick separation bubble size. The selection of the cases is made based on the histograms of Fig. 4, taking 10% of the realizations at the lower

end of the histogram, 10% in the middle, and 10% at the higher end. It is noted that for the incipient separations, the shallow case is made up of only attached realizations. For the selection of the medium and thick cases, only the part of the histogram corresponding to the separated flow cases is considered. This was done to eliminate a biasing of the results due to the large weight of the attached flow in the histogram. To this aim, the peak at zero was eliminated from the histogram. The medium bubble height was then based on 10% of the remaining realizations in the middle of the histogram and similarly the thick bubble height was defined based on 10% of the realizations at the higher end.

A. Development of Mean Separation

Based on the selection of bubble heights described above, the following mean flow results have been obtained (see Fig. 8). To highlight the development of the mean reversed flow region, only the negative mean U component is shown, with the shallow separation bubble case on the top and the thick bubble on the bottom. We consider first the incipient cases. Evidently, no mean flow reversal occurs for the lowest separation bubbles (shallow case), as all these realizations correspond to an attached flow. For the medium case, separation does occur instantaneously, but no mean flow reversal is observed. It is likely that these cases correspond to small pockets of separated flow that occur randomly in space. These pockets would not produce a mean flow reversal as a consequence of their random distribution in space. In fact, mean flow reversal only occurs for the thick separation bubble case. The fact that the same results are obtained for both incipient separation cases is another confirmation of their equivalence in interaction strength (see Sec. III).

Another observation is that all figures for the low Reynolds number case taken together seem to display a consistent increase in the extent of separation: with increasing interaction strength, the size of the separation bubble increases. Stated differently, the thick separation bubbles for the incipient cases (high Reynolds 6.0 deg, low Reynolds 5.5 deg) correspond approximately to the shallow separation bubbles for the 8.0 deg case. Similarly, the medium bubble of the 8.0 deg case falls between the shallow and the medium bubbles for the 9.5 deg case. Similarly, the thick bubble for 8.0 deg fits in between the medium and the thick bubbles for 9.5 deg. (The reader should consider that incipient separation plots use different scales for the vertical axis in Fig. 8.) It may be speculated that there is a spectrum of flow separation that develops as a function of the interaction strength. This suggests a continuous evolution of the mechanisms at work in the interaction, from an attached case to a fully separated configuration. The dominance of each mechanism depends on the strength of the interactions.

B. Correlation Between Shock Position and Bubble Height

It has been shown in Sec. IV that the reflected shock is unsteady in all cases. In the incipient cases, shock crossings occur near the edge of the boundary layer, and the estimation of L_{ex} was hence necessarily constrained to heights with $y/H > 1$. In this region, a length of excursion has been found of about $0.2L$, or $\approx 0.40\delta_0$. For the separated cases [11], L_{ex} was found to decrease from about $0.3L$ at the wall to $0.1L$ for $y/H = 1.6$. It is therefore quite difficult to conclude, based on the magnitude of L_{ex} alone, whether similar mechanisms can be associated with the shock movements between the incipient and separated cases. However, in the separated cases, the shock motions were found to be strongly linked with the bubble height [3]. In Sec. V.A it was shown that in the incipient cases, the separation bubble is nonexistent most of the time, even if spots of reverse flow occur. Nevertheless, a bubble of rather limited extent can

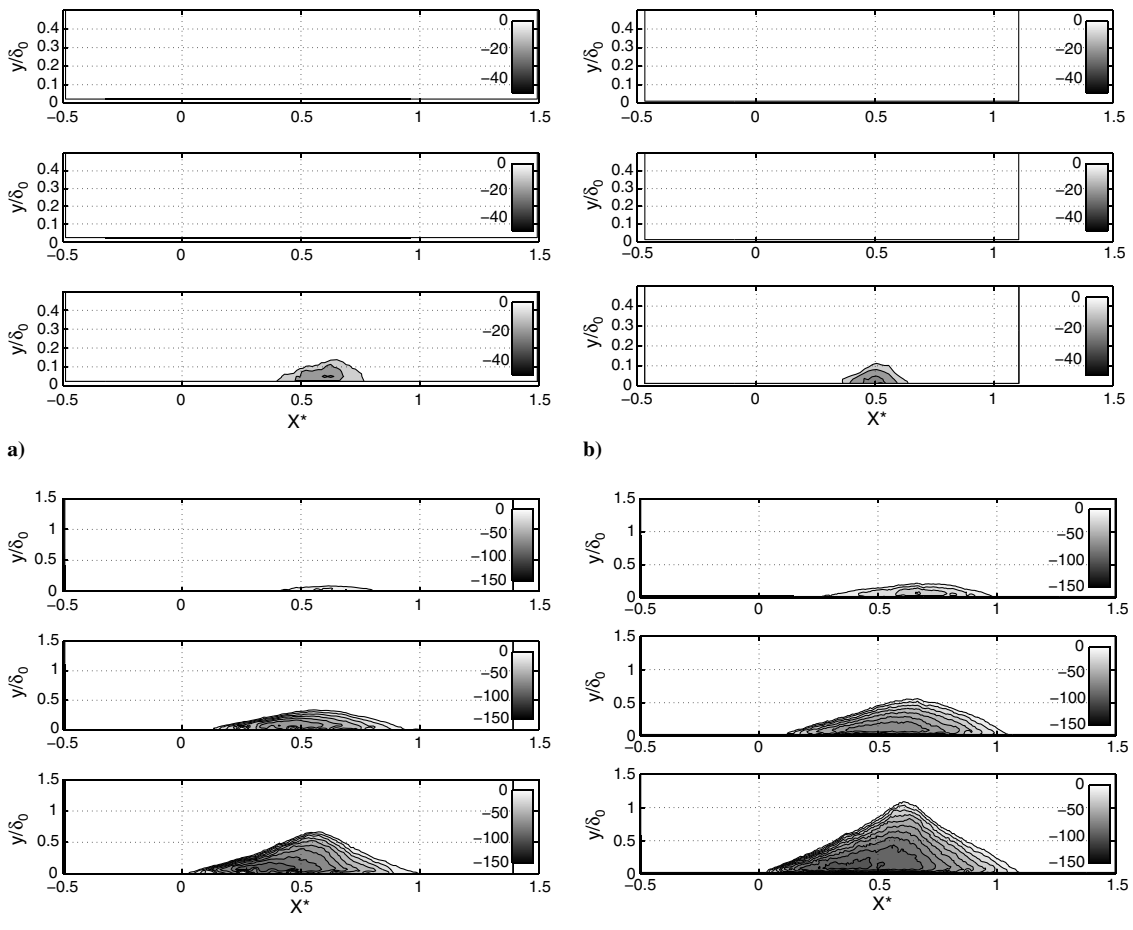

Fig. 8 Mean reversed flow (U component): high Reynolds number a) 6.0 deg, low Reynolds number b) 5.5 deg, and low Reynolds number separated cases c) 8.0 and d) 9.5 deg, from previous work [3].

develop in rare cases. Therefore, it is of interest to check if all, or at least a part, of the shock unsteadiness can be related to the unsteady flow reversal as in the separated interactions.

To determine the correlation between the state of the separation region and the position of the reflected shock, the conditional turbulent velocity fields are considered. The shock position is deduced from the longitudinal evolution of the V-component fluctuations: its mean conditional position is associated to the peak of the conditional RMS values. The results are reported in Fig. 9. To take into account the different aspect ratios of the interaction (H/L, see Table 2) between the high and low Reynolds number, the comparisons between the different interactions are made at the same nondimensional height (y/H): positions for $y/H > 1$ correspond to the flow above to the shock crossing point. The peak that is observed upstream of the reflected shock corresponds to the incident shock. It is clear that for both incipient cases, no particular motion of the reflected shock can be related with shallow or medium bubble states. For the latter this is a direct consequence of the hypothesized randomly occurring pockets of separation (see Sec. V.A), which cannot be expected to cause a consistent upstream displacement of the reflected shock. When a separation bubble is formed (thick bubble case), a slight correlation between the bubble height and the shock displacement appears for the high Reynolds case. Nevertheless, the amplitude of the motion is smaller than for the separated interactions (about $0.05L$ and even smaller for the low Reynolds incipient case, compared with $0.1L$ for the separated cases). The opposite tendency is observed for the total extent of the shock oscillations ($0.2L$ in the incipient cases compared with $0.1L$ for separated cases). Hence, the magnitude of the shock displacements linked to the bubble pulsations represent 25% of the total shock excursion amplitude, to be compared with about 100% in the separated cases. Therefore, when an instantaneous bubble is developed it seems that the incipient cases do present behavior similar to the separated cases, despite a reduced order of magnitude in the effect.

C. Correlation Between Incoming Boundary Layer and Bubble Height

To complete the comparisons between incipient and separated cases, conditional statistics have been carried out in the upstream boundary layer. They are based on the same classes as for the conditional bubble statistics. The upstream velocity profiles for the three instantaneous bubble states (shallow, medium, and thick bubbles) are shown in Fig. 10.

For the separated interactions, no significant correlation between the different states of the bubble was found, see Figs. 10c and 10d. In the incipient cases, on the contrary, a correlation, although rather limited, can be observed: the shallow and medium bubbles correspond to fuller profiles than the thick bubbles, the difference amounting up to 5% of the local velocity. As the expected uncertainty in the PIV mean velocity measurements is less than 1% of the velocity, the effect can be considered significant. Again, no dependence on the Reynolds number is observed. Consequently, it seems that in the incipient cases, the upstream boundary layer is more involved in the unsteadiness of the interaction zone. Therefore, the incipient case appears as an intermediate case between a fully attached interaction, where shock unsteadiness is expected to be governed by the turbulent structures of the upstream boundary layer, and a separated interaction, where they are mostly related to the downstream unsteadiness developing in the interaction region.

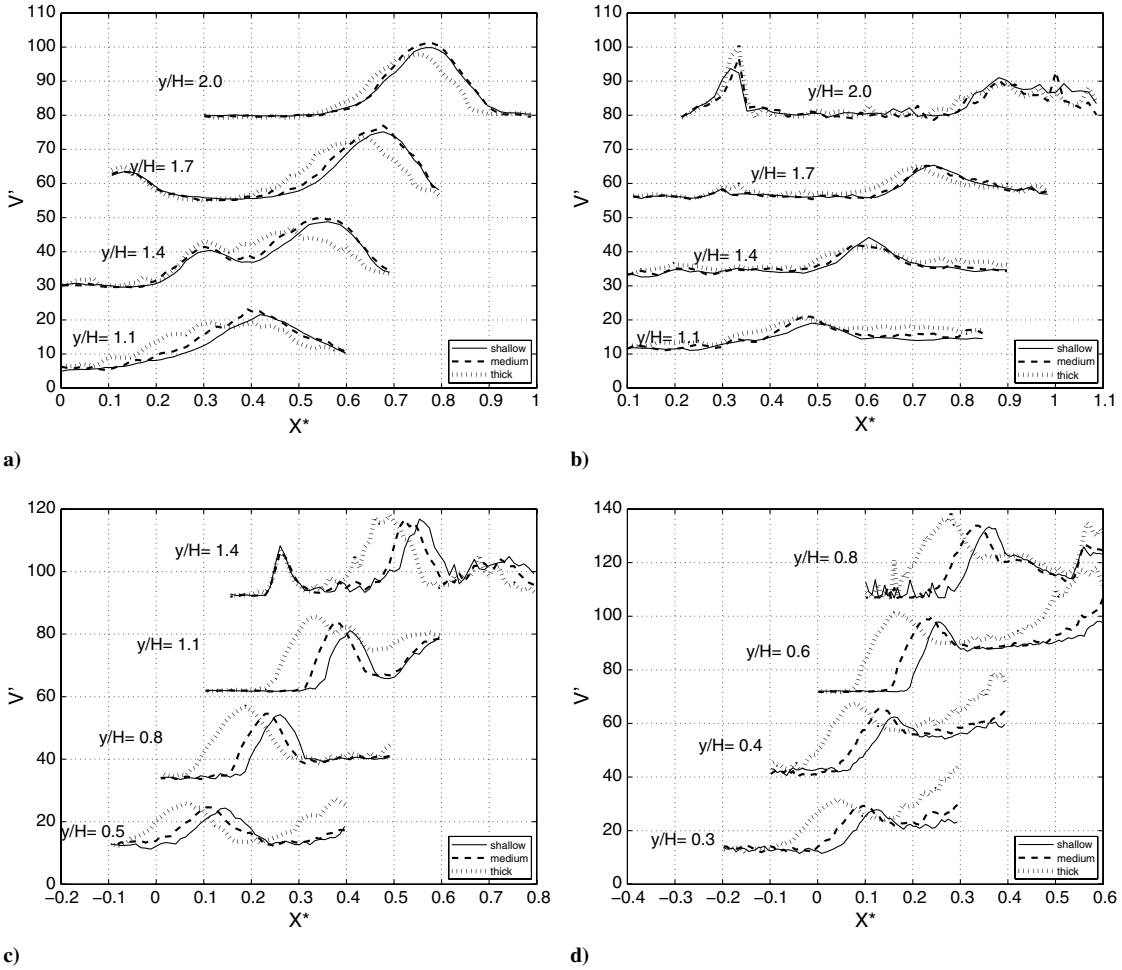

Fig. 9 Conditional shock position, defined as the maximum of the conditional normal velocity standard deviation: high Reynolds number a) 6.0 deg, low Reynolds number b) 5.5 deg, and low Reynolds number separated cases c) 8.0 and d) 9.5 deg. Separated cases have been reported in previous work [3].

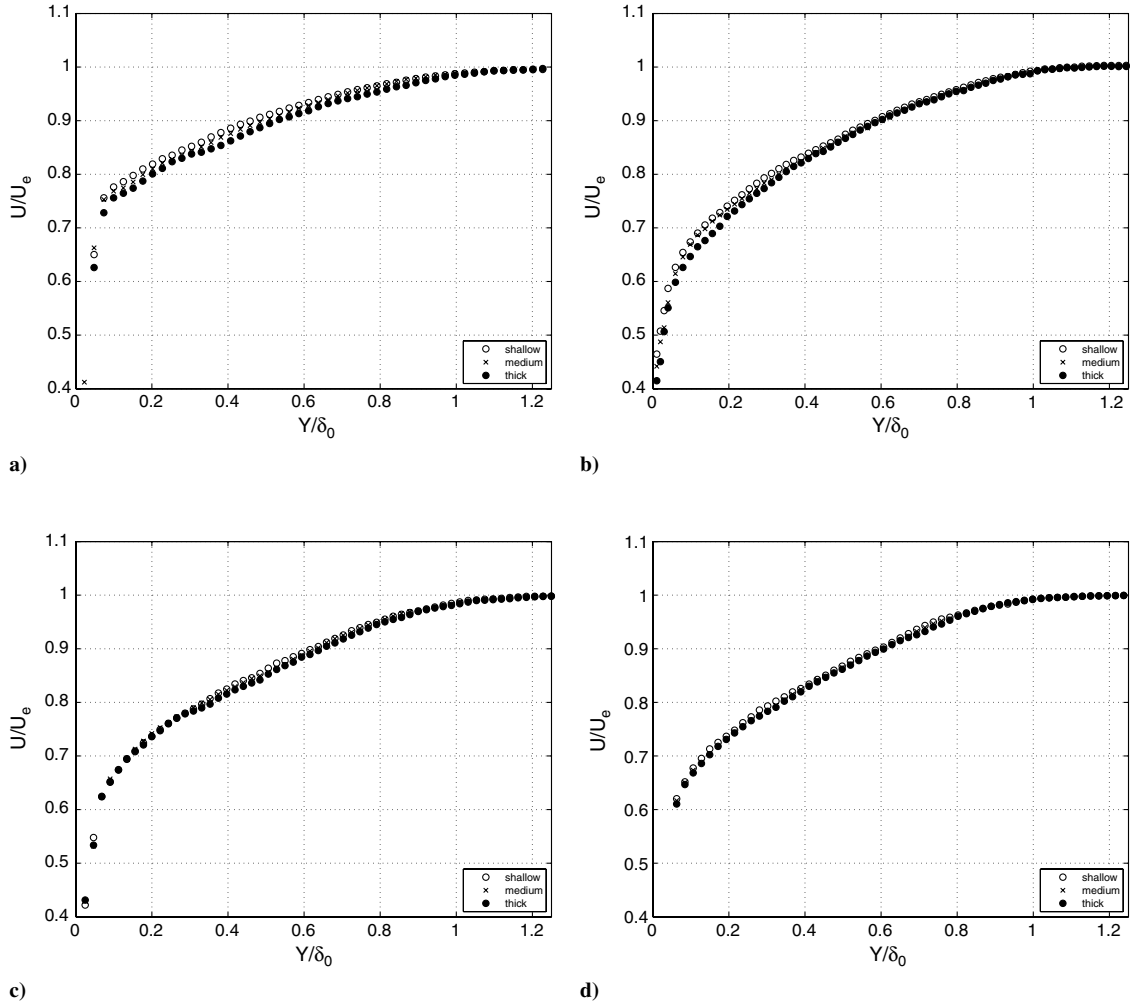

Fig. 10 Conditional mean velocity in the upstream boundary layer (U component): high Reynolds number a) 6.0 deg, low Reynolds number b) 5.5 deg, and low Reynolds number separated cases c) 8.0 and d) 9.5 deg, from previous work [3].

Accordingly, it should be expected that the associated time scales differ significantly between the incipient and the separated cases. Indeed, it has been shown that in shock-induced separation, the characteristic shock frequency f_s is such that the Strouhal number equals $S_L = \frac{f_s L}{U_1} \approx 0.03$ for a Mach number of $M > 2$ and for a wide range of geometries [34]. On the contrary, such well-defined low-frequency content has not been observed in the low Reynolds incipient case, which exhibits broadband spectra in the vicinity of the reflected shock [3]: there exists a low-frequency content in the range of $S_L \approx 0.03$, but it does not contribute to the main part of the energy of the signals related to the shock unsteadiness. This confirms again that, if similar mechanisms are present in both types of interactions, they do not occur with a similar importance.

D. Correlation Between Vortex Shedding Layer and Bubble Height

It has been shown in the previous sections that the different interactions exhibit very similar properties, mainly the development of energetic structures downstream of the reflected-shock foot, which has been observed in all cases. When mean separation occurs, it is classical to relate this to the development of a mixing layer and the creation of large vortical structures. This is generally associated with typical velocity profiles with a generalized inflection point. It is not intuitively straightforward to expect that such properties can be observed when no separation occurs. The existence and origin of large vortical structures in the incipiently separated interactions will therefore be investigated here in more detail.

Figure 11 shows the velocity profiles obtained for the different interaction cases at the station $X^* = 0.25$, which corresponds approximately to the middle of the development of the suspected mixing layer. This corresponds to the region of high levels of turbulence: $y/L < 0.2$ for the well-separated interactions and $y/L < 0.1$ for the incipient cases (see Fig. 6). The upper boundary of the regions of elevated turbulence levels are indicated by the vertical solid lines in Fig. 11. Both separated cases display, as expected, velocity profiles similar to those observed in mixing layers for $y/L < 0.2$. The incipient cases also show profiles that display some resemblance in the domain $y/L < 0.1$. Therefore, in the incipient cases the possibility exists to develop vortical structures, as in the separated cases.

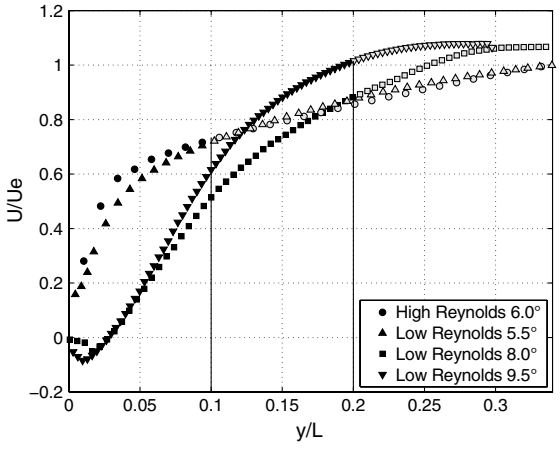

Fig. 11 Dimensionless velocity profile for $X^* = 0.25$.

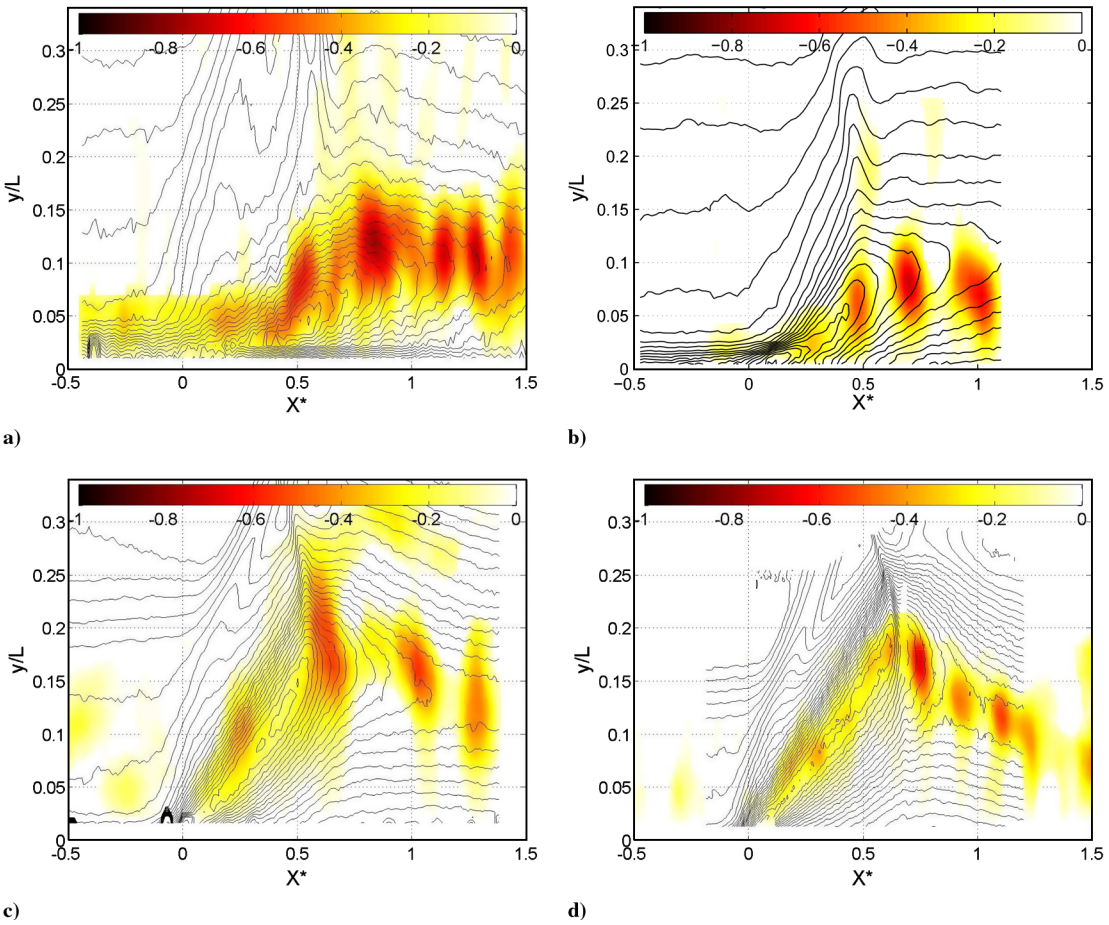

Fig. 12 Instantaneous visualizations of the mixing layer with consecutive vortex shedding: high Reynolds number a) 6.0 deg, low Reynolds number b) 5.5 deg, and low Reynolds number separated cases c) 8.0 and d) 9.5 deg. Isocontours of the *U*-component fluctuations (see Fig. 6) are shown for reference.

To highlight the existence of such vortical structures, a vortex detector has been applied on the instantaneous PIV velocity fields. It is based on a nonlocal criterion [35], and has been found efficient for extracting the large coherent structures in the separated cases [23]. It is defined in the following way. Let P be a point of the vector field, S a two-dimensional area surrounding P, and M a point of this area. The vorticity detector Γ_1 is defined as

$$\Gamma_1(P) = \frac{1}{S}\int_{M\in S} \frac{(\boldsymbol{PM}\times\boldsymbol{U}_M)\cdot z}{\|\boldsymbol{PM}\|\cdot\|\boldsymbol{U}_M\|}\,\mathrm{d}S = \frac{1}{S}\int_S \sin\theta_M\,\mathrm{d}S \simeq \frac{1}{N}\sum_N \sin\theta_M \tag{1}$$

where $\boldsymbol{U}_M$ is the local velocity at the point M, z is the unit vector normal to the measurement plane, θ_M is the angle between the two vectors $\boldsymbol{PM}$ and $\boldsymbol{U}_M$, and N is the number of PIV vectors in the area S. This criterion has values between -1 and 1, and it can be shown that the values of $|\Gamma_1| > 2/\pi$ correspond to the presence of a vortex, with the sign of Γ_1 related to the direction of rotation.

Typical instantaneous fields of the vortex detector are reported in Fig. 12. The isocontour of the U-component fluctuations have been superimposed onto the figure. It is clear that the regions of high turbulence levels are directly related to the development of a mixing layer downstream of the reflected-shock foot. This does not depend on the existence of an instantaneous bubble of recirculation in the incipient cases: the examples shown in Figs. 12a and 12b correspond to realizations without flow separation, belonging to the case $h = 0$ in Figs. 4a and 4b. This is confirmed by the map of the mean vortex detector, computed on the whole data set (see Fig. 13). Whatever the flow, similar average values are obtained, which shows that there is the same probability to observe large vortical structures.

VI. Discussion

From the different experimental results presented, some general features of the flow organization and the unsteadiness mechanisms developing in the shock boundary-layer interactions can be deduced for the case of the incident shock reflection. First of all, it appears that the Reynolds number effect acts mainly on the length scale L of the interaction. Another important Reynolds number effect concerns the properties of the reflected shock in the turbulent part of the boundary layer. It appears significantly less well-defined in the low Reynolds case for incipient separation, and it should consequently be considered rather as a fan of compression waves. This is in accordance with the behavior that has been reported in the case of compression ramps. Nevertheless, when similar interactions are considered, based on the intensity of the reversed flow, the unsteadiness observed in the interactions presents a large resemblance whatever the Reynolds number.

Concerning the unsteadiness mechanisms, it has been shown previously that in the case of separated interactions, the low-frequency shock dynamics are strongly correlated with the separation bubble pulsation. In the current work, two incipient cases were considered, without mean separation but with a large probability of instantaneous flow reversal. This has been done for Reynolds numbers based on the momentum thickness of, respectively, 5000 and 50,000. In both cases, the development of large coherent structures downstream of the reflected-shock foot has been demonstrated, with a very similar behavior as compared with the separated cases. At the same time it has been shown that, despite the absence of mean separation, intermittent recirculation bubbles do occur, but with a very low probability (less than 4% of the realizations). In the case of such an event, correlations with the reflected-shock movements have been observed, analogous to the fully separated interactions. At the same time, a slight correlation with the

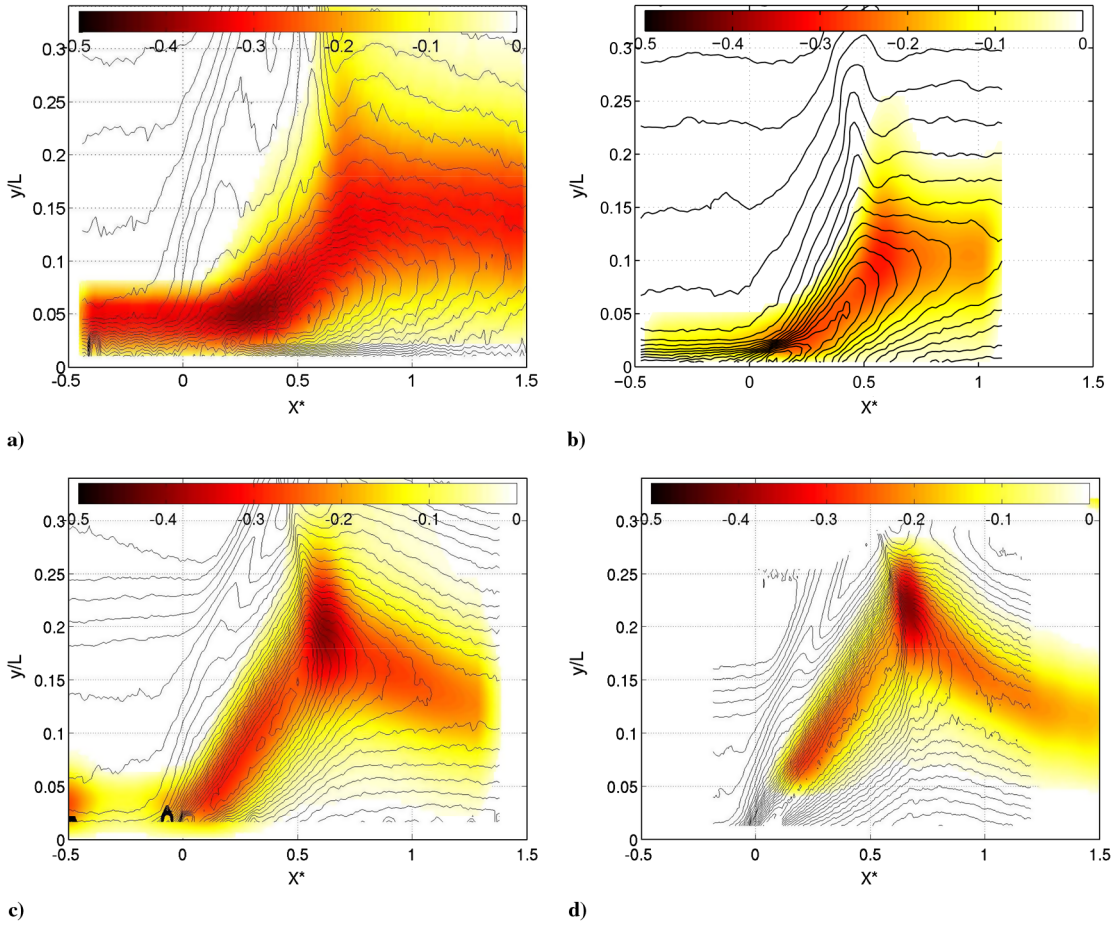

Fig. 13 Average of the visualizations of the mixing layer with consecutive vortex shedding: high Reynolds number a) 6.0 deg, low Reynolds number b) 5.5 deg, and low Reynolds number separated cases c) 8.0 and d) 9.5 deg. Isocontours of the *U*-component fluctuations (see Fig. 6) are shown for reference.

upstream boundary-layer profile fullness has been observed. This dependence of the separation bubble on the upstream boundary layer, notwithstanding the fact that it is rather limited, is larger than for the separated cases. Therefore, it seems that similar mechanisms are present in both cases (separated or incipient), independent of the Reynolds number. On the contrary, the predominance of a mechanism for the shock unsteadiness (upstream state, downstream separation bubble dynamics) appears to depend on the mean state of the interaction. Accordingly, the resulting frequency spectrum of the overall unsteadiness can be considered as the consequence of different characteristic times scales with a weighting function depending on the state of the flow:

1) When no separation occurs at all, upstream events are expected to govern the flow unsteadiness, with rather high frequencies.

2) When separation occurs most of the time, downstream unsteadiness, related to the separated bubble pulsation, will become predominant and involve very low frequencies.

3) Finally, for the incipient cases, there is a superposition of different mechanisms, involving time scales that can differ by at least one decade; this will produce spectra that are more or less similar to separated ones, depending on the probability of the occurrence of instantaneous flow separation.

The influence of the Reynolds number on the flow unsteadiness appears rather limited for turbulent SWBLIs. Very similar results have been obtained in the low Reynolds supersonic facility at the IUSTI and the high Reynolds facility at the TU Delft, when similar interactions based on the flow separation probability are considered.

Acknowledgments

The current research was supported by the Research Pole ONERA/Centre National d'Etudes Spatiales *Aérodynamique des Tuyères et Arrière-Corps* and by the European Commission in the context of the 6th Framework Program UFAST ("Unsteady Effects of Shock Wave Induced Separation"). This work constitutes a cooperation between TU Delft and the Groupe Supersonique of the IUSTI (Unité Mixte de Recherche, Centre National de la Recherche Scientifique 6595) in Marseille. The author wishes to gratefully acknowledge the input, ideas, and support of both institutions.

References

[1] Dolling, D. S., "Fifty Years of Shock-Wave/Boundary-Layer Interaction Research: What Next," *AIAA Journal*, Vol. 39, No. 8, Aug. 2001, pp. 1517–1531. doi:10.2514/2.1476

[2] Doerffer, P., "European Research on Unsteady Effects of Shock Wave Induced Separation UFAST Project," *Proceedings of the 8th International Symposium on Experimental and Computational Aerothermodynamics of Internal Flows*, Lab. de Mécanique des Fluides et d'Acoustique, Ecole Centrale de Lyon, Lyon, France, July 2007, pp. 1–6.

[3] Piponniau, S., Dussauge, J. P., Debiève, J. F., and Dupont, P., "A Simple Model for Low-Frequency Unsteadiness in Shock-Induced Separation," *Journal of Fluid Mechanics*, Vol. 629, 2009, pp. 87–108. doi:10.1017/S0022112009006417

[4] Beresh, S. J., Clemens, N. T., and Dolling, D. S., "Relationship Between Upstream Turbulent Boundary Layer Velocity Fluctuations and Separation Shock Unsteadiness," *AIAA Journal*, Vol. 40, No. 12, Dec. 2002, pp. 2412–2422. doi:10.2514/2.1609

[5] Ganapathisubramani, B., Clemens, N. T., and Dolling, D. S., "Effects of Upstream Boundary Layer on the Unsteadiness of Shock-Induced Separation," *Journal of Fluid Mechanics*, Vol. 585, 2007, pp. 369–394. doi:10.1017/S0022112007006799

[6] Ganapathisubramani, B., Clemens, N. T., and Dolling, D. S., "Low-Frequency Dynamics of Shock-Induced Separation in a Compression

Ramp Interaction," *Journal of Fluid Mechanics*, Vol. 636, 2009, pp. 397–425.
doi:10.1017/S0022112009007952

[7] Humble, R. A., Elsinga, G. E., Scarano, F., and Van Oudheusden, B. W., "Three-Dimensional Instantaneous Structure of a Shock Wave/Turbulent Boundary Layer Interaction," *Journal of Fluid Mechanics*, Vol. 622, 2009, pp. 33–62.
doi:10.1017/S0022112008005090

[8] Plotkin, K. J., "Shock Wave Oscillation Driven by Turbulent Boundary Layer Fluctuations," *AIAA Journal*, Vol. 13, No. 8, 1975, pp. 1036–1040.
doi:10.2514/3.60501

[9] Erengil, M. E., and Dolling, D. S., "Unsteady Wave Structure near Separation in a Mach 5 Compression Ramp Interaction," *AIAA Journal*, Vol. 29, No. 5, May 1991, pp. 728–735.
doi:10.2514/3.10647

[10] Thomas, F. O., Putman, C. M., and Chu, H. C., "On the Mechanism of Unsteady Shock Oscillation in Shock Wave/Turbulent Boundary Layer Interaction," *Experiments in Fluids*, Vol. 18, Nos. 1–2, 1994, pp. 69–81.
doi:10.1007/BF00209362

[11] Dupont, P., Haddad, C., and Debiève., J. F., "Space and Time Organization in a Shock Induced Boundary Layer," *Journal of Fluid Mechanics*, Vol. 559, 2006, pp. 255–277.
doi:10.1017/S0022112006000267

[12] Pirozzoli, S., and Grasso, F., "Direct Numerical Simulation of Impiging Shock Wave/Turbulent Boundary Layer Interaction at $M = 2.25$," *Physics of Fluid*, Vol. 18, No. 6, 2006, pp. 1–17.
doi:10.1063/1.2216989

[13] Wu, M., and Martin, M. P., "Direct Numerical Simulation of Supersonic Turbulent Boundary Layer over a Compression Ramp," *AIAA Journal*, Vol. 45, No. 4, April 2007, pp. 879–889.
doi:10.2514/1.27021

[14] Wu, M., and Martin, M. P., "Analysis of Shock Motion in Shockwave and Turbulent Boundary Layer Interaction Using Direct Numerical Simulation Data," *Journal of Fluid Mechanics*, Vol. 594, Jan. 2008, pp. 71–83.
doi:10.1017/S0022112007009044

[15] Touber, E., and Sandham, N. D., "Large-Eddy Simulation of Low-Frequency Unsteadiness in a Turbulent Shock-Induced Separation Bubble," *Theoretical and Computational Fluid Dynamics*, Vol. 23, No. 2, 2009, pp. 79–107.
doi:10.1007/s00162-009-0103-z

[16] Alizard, F., and Robinet, J. Ch., "Influence of 3D Perturbations in Separated Flows," *Proceedings of the IUTAM Symposium on Unsteady Separated Flows and Their Control*, IUTAM Book Series, Springer–Verlag, London, 2008, p. xvi.

[17] Ehrenstein, U., and Gallaire, F., "Two-Dimensional Global Low-Frequency Oscillations in a Separating Boundary-Layer Flow," *Journal of Fluid Mechanics*, Vol. 614, 2008, pp. 315–327.
doi:10.1017/S0022112008003285

[18] Souverein, L. J., Van Oudheusden, B. W., Scarano, F., and Dupont, P., "Unsteadiness Characterisation in a Shock Wave Turbulent Boundary Layer Interaction Through Dual-PIV," *38th Fluid Dynamics Conference and Exhibit*, AIAA Paper 2008-4169, Seattle, WA, 23–26 June 2008.

[19] Souverein, L. J., Van Oudheusden, B. W., Scarano, F., and Dupont, P., "Application of a Dual-Plane Particle Image Velocimetry (Dual-PIV) Technique for the Unsteadiness Characterization of a Shock Wave Turbulent Boundary Layer Interaction," *Measurement Science and Technology*, Vol. 20, No. 7, July 2009, pp. 074003.
doi:10.1088/0957-0233/20/7/074003 (16pp).

[20] Ginoux, J. J., "Interaction Entre Ondes de Choc et Couches Limites," *Chocs et Ondes de Choc, Tome 2*, edited by A. L. Jaumotte, Masson and Cie, Paris, 1973, pp. 1–65.

[21] Ragni, D., Schrijer, F., Van, B. W., Oudheusden, and F. Scarano, "On the Determination of PIV Particle Tracers Response Time by Shock Wave Tests," *8th International Symposium on Particle Image Velocimetry: PIV '09*, Paper PIV09-0130, Melbourne, Australia, 25–28 Aug. 2009.

[22] Scarano, F., and Riethmuller, M. L., "Iterative Multigrid Approach in PIV Image Processing With Discrete Window Offset," *Experiments in Fluids*, Vol. 26, No. 6, 1999, pp. 513–523.
doi:10.1007/s003480050318

[23] Dupont, P., Piponniau, S., Sidorenko, A., and Debiève, J. F., "Investigation of an Oblique Shock Reflection with Separation by PIV Measurements," *AIAA Journal*, Vol. 46, No. 6, June 2008, pp. 1365–1370.
doi:10.2514/1.30154

[24] Elena, M., Tedeschi, G., and Gouin, H., "Motion of Tracer Particles in Supersonic Flows," *Experiments in Fluids*, Vol. 26, No. 4, 1999, pp. 288–296.
doi:10.1007/s003480050291

[25] Smits, A. J., and Dussauge, J. P., *Turbulent Shear Layers in Supersonic Flow*, 2nd ed., Springer–Verlag, New York, 2006.

[26] Délery, J. M., and Marvin, J. G., "Shock Wave: Boundary Layer Interactions," AGARD, NATO TR 280, Neuilly-sur-Seine, France, 1986.

[27] Kiya, M., and Sasaki, K., "Structure of a Turbulent Separation Bubble," *Journal of Fluid Mechanics*, Vol. 137, 1983, pp. 83–113.
doi:10.1017/S002211208300230X

[28] Cherry, N. J., Hillier, R., and Latour, M. E. M., "Unsteady Measurements in a Separated and Reattaching Flow," *Journal of Fluid Mechanics*, Vol. 144, 1984, pp. 13–46.
doi:10.1017/S002211208400149X

[29] White, F. M., *Viscous Fluid Flow*, 2nd ed., McGraw–Hill, New York, 1991.

[30] Ringuette, M. J., Bookey, P., Wyckham, C., and Smits, A. J., "Experimental Study of a Mach 3 Compression Ramp Interaction at $Re_\theta = 2400$," *AIAA Journal*, Vol. 47, No. 2, Feb. 2009, pp. 373–385.
doi:10.2514/1.38248

[31] Ringuette, M. J., Wu, M., and Martin, M. P., "Low Reynolds Number Effects in a Mach 3 Shock/Turbulent-Boundary-Layer Interaction," *AIAA Journal*, Vol. 46, No. 7, July 2008, pp. 1884–1887.
doi:10.2514/1.36213

[32] Elsinga, G. E., Van Oudheusden, B. W., and Scarano, F., "Evaluation of Optical Distortion Effects in PIV," *Experiments in Fluids*, Vol. 39, No. 2, 2005, pp. 246–256.
doi:10.1007/s00348-005-1002-8

[33] Elsinga, G. E., Van Oudheusden, B. W., and Scarano, F., "The Effect of Particle Image Blur on the Correlation Map and Velocity Measurement in PIV," *Optical Engineering and Instrumentation, SPIE Annual Meeting*, SPIE Paper 5880-37, San Diego, CA, 31 July–4 Aug. 2005.

[34] Dussauge, J. P., Dupont, P., and Debiève, J. F., "Unsteadiness in Shock Wave Boundary Layer Interactions with Separation," *Aerospace Science and Technology*, Vol. 10, No. 2, 2006, pp. 85–91.
doi:10.1016/j.ast.2005.09.006

[35] Graftieaux, L., Michard, M., and Grosjean, N., "Combining OIV, POD and Vortex Identification Algorithms for the Study of Unsteady Turbulent Swirling Flows," *Measurement Science and Technology*, Vol. 12, Aug. 2001, pp. 1422–1429.
doi:10.1088/0957-0233/12/9/307

[36] Klebanoff, P. S., "Characteristics of Turbulence in a Boundary Layer with Zero Pressure Gradient," NASA TR 1247, 1955.

P. Givi
Associate Editor